# Assessment of Incompressible Turbulent Flow Over a Curved Hill with Passive Scalar Transport

David Paeres[1,*], Christian Lagares[1,†] and Guillermo Araya[1,‡]
[1]*HPC and Visualization Lab, Dept. of Mechanical Eng., University of Puerto Rico at Mayaguez, PR 00681, USA.*

**In the scenario of a curved hill, the main objective is to study a turbulent boundary layer for incoming horizontal turbulent airstream at 20 $m/s$ by reproducing the wind-tunnel geometry as in [1]. A two-dimensional CFD RANS is performed with scope in the curved hill where moderate and strong pressure gradients (both, favorable and adverse) are observed. We validate the incoming flow conditions with published Direct Numerical Simulation (DNS) and focus on comparisons with experimental data by Baskaran *et al.* [1] for the curved hill. The simulations leveraged the open-source software OpenFOAM® and compared two turbulence models, the $K-\omega$ SST and the Spalart-Allmaras. The thermal field is included and assumed a passive scalar (i.e., buoyancy forces are neglected). Additionally, the passive scalar transport (with a molecular Prandtl number of 0.71) is validated against DNS database at moderate Reynolds numbers. Further, identifying the edge of the boundary layer's edge becomes nontrivial under strong pressure gradients caused by wall curvature where the BL becomes significantly distorted and can experience strong acceleration/deceleration and higher peak velocities than that of the freestream. In the present work, we follow a more theoretical approach to identifying the edge of the boundary layer based on a potential flow solution in the same domain. This leads to more consistent results without the need for corrections considering pressure gradients. The results exhibit very good agreement with the data published by Baskaran *et al.* [1]. The SA model shows better agreement with the experimental baseline on wall parameters whereas the $K-\omega$ SST has a slight edge on the transition to the adverse pressure gradient (APG) region in terms of its wall pressure prediction which leads to a superior prediction of the separation point over the SA model, which possesses a small delay in this prediction. Nonetheless, the SA model exhibits a superior performance in the presence of strong surface curvature induced favorable pressure gradient (FPG) where, we hypothesize, the flow experiences a quasi-laminarization process. Nonetheless, more information is certainly required to confirm the presence (or lack thereof) of a laminarescent state at the top of the hill.**

## I. Nomenclature

| | | |
|---|---|---|
| APG | = | Adverse Pressure Gradient |
| CFD | = | Computational Fluid Dynamics |
| $E$ | = | Rate of deformation |
| $\epsilon$ | = | Turbulent energy dissipation ratio |
| FPG | = | Adverse Pressure Gradient |
| $K$ | = | Turbulent kinetic energy |
| $k$ | = | Thermal conductivity or vector index (we disambiguate as required throughout the text) |
| $\mu$ | = | Molecular dynamic viscosity |
| $\mu_t$ | = | Turbulent dynamic viscosity |
| $\nu$ | = | Molecular kinematic viscosity |
| $\nu_t$ | = | Turbulent kinematic viscosity |
| $\omega$ | = | Turbulent energy specific dissipation ratio |
| $Pr$ | = | Prandtl number |

*MSc Student and Research Assistant, AIAA Student Member
†Doctoral Candidate and Research Assistant, AIAA Student Member
‡Associate Professor, AIAA Associate Fellow, araya@mailaps.org

RANS = Reynolds-Averaged Navier-Stokes
$\rho$ = Density
$S$ = Source term
SA = Spalart Allmaras turbulent model
SST = $K-\omega$ Shear Stress Transport turbulent model
$T$ = Temperature
$t$ = Time
$\tau$ = Shear Stress
$U$ = Instant velocity vector
$u$ = Instant streamwise velocity component
v = Instant vertical velocity component
$w$ = Instant cross-flow velocity component
$X$ = Spatial position vector
ZPG = Zero Pressure Gradient
$\bar{()}$ = Average notation
$()'$ = Fluctuation notation

$\alpha_\omega, \beta, \beta*, \beta_2, \kappa, \sigma, \sigma*, \sigma_K, \sigma_v, \sigma_\epsilon, \sigma_{\omega 1}, \sigma_{\omega 2}, C_{1\epsilon}, C_{2\epsilon}, C_{b1}, C_{b2}, C_{w1}, \gamma_2$ = Turbulent models constant coefficients

# II. Introduction

## A. Scope of present work

There is still much to understand in the science of Computational Fluid Dynamics (CFD) for turbulent flows, particularly, in the aspects of wall curvature effects with passive scalar transport. Describing this type of flow as "unpredictable" carries much weight as a mystery, so it is more appreciable in the present day to use the word "chaotic" instead. Still, chaos requires to be explained in a more emphatic way to strangers of this science. However, solving this issue will not occur in this work.

In the case of turbulent flow over a curved hill, separation zones will occur due to the strong Adverse Pressure Gradient (APG) or flow deceleration caused by the presence of convex wall curvature. An incoming horizontal airstream at 20 $m/s$ passing over a simple curved protuberance of 1.284 meters long with radios of 1.08 meters from the experiments of Baskaran et al.[1] is considered as a validation tool. To this scenario, a 2D numerical assessment will be performed with scope to the flow's separation zone velocity and with the presence of temperature in the simulation as a passive scalar. First, a fundamental literature review will be carried out for flow separation by wall curvature and standard turbulent models. The numerical approach will be using a RANS (Reynolds-Averaged Navier-Stokes) model. Using open-source CFD software OpenFOAM®, the velocity field will be solved in the scenario of considering a molecular Prandtl of 0.71 (i.e., air as the working fluid) and two turbulent models *$K-\omega$ Shear Stress Transport (SST) [2] and Spalart-Allmaras (SA) [3]*. The inclusion of temperature is done based on the theory of passive scalar transport as in [4]. Results obtained will be discussed to finally present recommendations for future work improvement in this study.

## B. Background

Numerically solving turbulent flows requires much computational power, and these are resources not easy to have handy. Therefore, formulating models that significantly reduce the computational power requirement and maintain high precision between results and proper solution is a simply appreciable benefit. Among the existing CFD categories, the most commonly known are RANS (Reynolds-Averaged Navier-Stokes), LES (Large Eddy Simulation) and DNS (Direct Numerical Simulation) [5]. As stated in the name, DNS directly solves the governing formulation of all fluid flows called the Navier-Stokes equations; it does not use turbulent models and requires significant computational resources. As a consequence, if one desires to perform DNS is mandatory to employ a highly scalable and efficient flow solver, not to mention if the idea is to predict spatially-developing turbulent boundary layers (SDTBL) implying accurate turbulent time-dependent inflow conditions. Therefore, DNS requires researcher's skills, expertise and abilities on HPC and parallel programming not only during the running but also in the postprocessing stage [6]. With the advent of powerful supercomputers, it has becomes easier to push the boundaries of turbulent boundary layer simulations at higher Reynolds number via DNS [7], [8]. On the other hand, LES models the dynamics and influence of

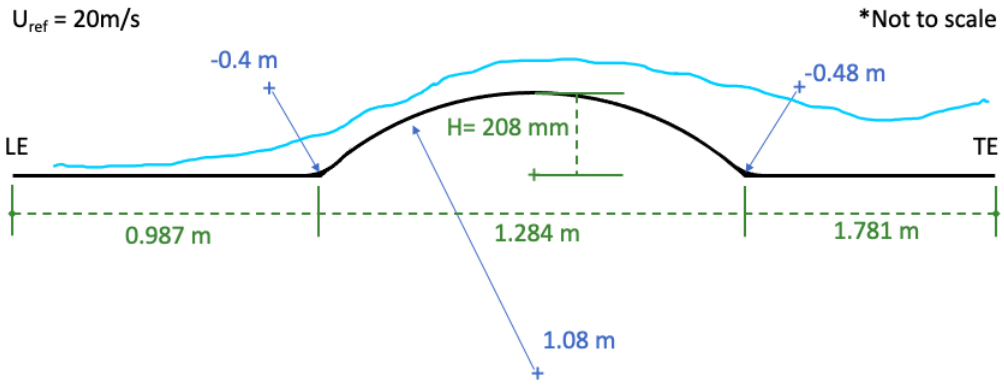


**Fig. 1 Curved hill diagram (partially reproduced from [1].**

Kolmogorov scales but is reasoned in using a borderline as a spatial filter; large-scale motions (called large eddies) are computed directly, and only the small-scale motions (considered eddies of thermal energy dissipation) are modeled, resulting in a significant reduction in computational resources compared to the DNS approach. However, this effort reduction depends on the analyzed geometry: it is well known that in wall-bounded flows even the "inertial subrange scales" located in the near wall region could be very small. Thus, the computing and running effort reduction by considering LES with respect to DNS could be limited to one order of magnitude, at most, according to present author's experience. Among these three categories, RANS is the approach where the simulation framework is highly simplified since the whole power spectra of flow fluctuations is modeled. Despite its simplicity and limitations on complex geometries, RANS may supply an important insight of the flow. Within RANS literature for turbulent flows, there are four most popularly used turbulent models, namely: $K-\epsilon$, Standard $K-\omega$, $K-\omega$ Shear Stress Transport and Spalart-Allmaras.

The term flow separation does not always mean that the actual fluid untouches the body flowing on. Most of the time, this detachment is regarding when the flow's boundary layer abruptly modifies interactions with the body. Flow separation happens when decelerated fluid flows around bodies, detaches causing the fluid closest to the object's surface to flow in reverse or different directions from the streamwise. This event most often gives rise to turbulent fluctuations, causing their enhancement. It is essential to highlight that flow separation can be induced either by geometrical singularities, for example, in the presence of sharp corners, or by smooth geometry variations, as those occurring over a curved wall [9]. The mere presence of a very strong adverse pressure gradient (APG), depending on the magnitude, might be sufficient to cause flow detachment.

The inspiration of the assessment presented here is from the experimental work of Baskaran et al. [1]. In their work, a horizontal air stream at 20 $m/s$ passed over a simple curved convex hill of 1.284 meters long with radios of 1.08m. The protuberance's entrance and exit had a concave surface of -0.40m and -0.48m, respectively. Figure (1) shows an example of the geometries. In [1], the momentum boundary layer parameters (first and second-order statistics) were measured. Boundary layer thickness, displacement thickness, momentum thickness, and other integral parameters calculated were used to describe the flow's characteristics and behavior. Other relevant information, for example, streamwise pressure and skin friction at the wall, velocities profiles at specific streamwise locations, and Reynolds stresses, were also measured. Their main objective was "to study the response of turbulent boundary layers to sudden changes in surface curvature and pressure gradient" [1]. Although, the experimental data of the velocity field is used as a point of validation of our numerical approach. *It is worth highlighting that the present study also considers temperature as a passive scalar which was not explicitly accounted for in the original experiment.*

In summary and to the best of our knowledge, the combined effect of flow separation by wall curvature and the transport of temperature as passive scalar has not been fully addressed in the past or is relatively scarce.

## III. Formulations

### A. Reynolds Averaged Navier-Stokes Equation

The RANS models are based on the Boussinesq hypothesis [5] and the Reynolds decomposition, i.e., the mathematical notion that each instant property can be written as the sum of mean and fluctuations fields. Example $U = \bar{U} + U'$, being $U$ an instantaneous flow property, $\bar{U}$ the average of $U$ and $U'$ the fluctuations of $U$. So the mean flow field is solved; meanwhile, the fluctuations are estimated. For general compressible fluid flows [10], the governing equations are:

Conservation of mass

$$\frac{\partial \rho}{\partial t} + \nabla \cdot (\rho U) = 0 \tag{1}$$

Conservation of momentum, obtained from Navier-Stokes equations, where sub-index $i$ is for notation of vectors' component

$$\frac{\partial (\rho U_i)}{\partial t} + \nabla \cdot (\rho U_i U) = -\frac{\partial \rho}{\partial X_i} + \nabla \cdot (\mu \nabla U_i) + S_{Mi} \tag{2}$$

Conservation of passive scalar, being $e$ an scalar and assumed to follow a similar Navier-Stokes equation form

$$\frac{\partial (\rho e)}{\partial t} + \nabla \cdot (\rho e U) = \nabla \cdot (k \nabla T) + S_e \tag{3}$$

Where $S$ are the source terms. If the incompressibility assumption and the Reynolds decomposition is applied, the RANS models for Newtonian fluids have the following equations:

*Conservation of mass (Continuity equation)*

$$\rho \nabla \cdot \overline{U} = 0 \tag{4}$$

*Conservation of momentum*

$$\rho \frac{\partial \overline{U}}{\partial t} + \rho \nabla \cdot (\overline{UU}) = -\nabla \overline{P} + \left( \nabla \cdot (\overline{\tau} - \rho \overline{U'U'}) \right) + \overline{S_M i} \tag{5}$$

Note in equations (4) and (5) the emergence of new terms. In RANS, the mean parameters are computationally solved, but the fluctuations terms stay unknown. It is precisely here where the Boussinesq hypothesis acts, enabling models proposal for estimating the unknown terms and balancing the equations. Also, the density parameter at each partial derivative is pulled out due to the constant assumption of the incompressible condition.

### B. Turbulent Flow Models

As said in the introduction, there are four most popular RANS models used. To understand these models is essential to describe four important parameters briefly. The first and principal is called turbulent kinematic viscosity, generally written as $\nu_t$. Also known as eddy viscosity per density ($\mu_t / \rho$), it is responsible for identifying the correct energy dissipation due to flow turbulence based on Boussinesq postulated [10]. $\nu_t$ is an apparent property for viscosity but accounting for the turbulent phenomenon. The second parameter is the turbulent kinetic energy ($K$), which is the kinetic energy per unit mass of turbulent fluctuations and is mathematically defined by:

$$K \equiv \frac{1}{2} \overline{U_i' U_i'} = \frac{1}{2} (\overline{u'^2} + \overline{v'^2} + \overline{w'^2}) = \frac{3}{2} \overline{U'^2} \tag{6}$$

Third is the turbulent dissipation ratio ($\epsilon$), defining the ratio at which turbulent kinetic energy is converted to internal thermal energy. The mathematical description of $\epsilon$ is:

$$\epsilon \equiv \nu \overline{\frac{\partial U_i'}{\partial X_k} \frac{\partial U_i'}{\partial X_k}} \tag{7}$$

The last parameter is the specific turbulent dissipation ratio ($\omega$). $\omega$ is the ratio of the turbulent kinetic energy converted into internal thermal energy per unit of time and volume. For precisely having Hertz units, it is also known as frequency

**Table 1 Term's representation and constant coefficient values for $K-\epsilon$ model**

| $U_i$ | velocity components in notation | $\beta^*$ | $\sigma_K$ | $\sigma_\epsilon$ | $C_{1\epsilon}$ | $C_{2\epsilon}$ |
|---|---|---|---|---|---|---|
| $E_{ij}$ | rate of deformation | 0.09 | 1.00 | 1.30 | 1.44 | 1.92 |

**Table 2 Recommended values for the coefficients in Standard $K-\omega$ model**

| $\alpha_\omega$ | $\beta$ | $\beta^*$ | $\sigma$ | $\sigma^*$ |
|---|---|---|---|---|
| $\frac{5}{9}$ | $\frac{3}{40}$ | $\frac{9}{100}$ | $\frac{1}{2}$ | $\frac{1}{2}$ |

turbulence average. The relationship between $\omega$ to $K$ and $\epsilon$ is generally written as equation (8) where $\beta^*$ is a model constant that, for example, can be around 1.0 or even 0.09.

$$\omega = \frac{\epsilon}{K\beta^*} \tag{8}$$

The turbulent model $k-\epsilon$ initially proposed by Launder and Spalding [11] is considered a high Reynolds number model and this indicates that its specialty is in good results away from near-wall [12]. This model is uses the scalar conservation equation 3 to estimate $K$ and $\epsilon$. In essence, says that *the rate of change of K (or $\epsilon$) plus the transport of K (or $\epsilon$) by convection is equal to the transport of K (or $\epsilon$) by diffusion plus the production rate of K (or $\epsilon$) minus the destruction ratio of K (or $\epsilon$).* The estimations are performed following equations (10) for $K$ and for $\epsilon$ the equation (11). Then, the eddy viscosity ($\mu_t$) is calculated with the equation (9) where the constants' common values use are contained in table 1.

$$\mu_t = \frac{\nu_t}{\rho} = \frac{\beta^* K^2}{\epsilon} \tag{9}$$

$$\frac{\partial(\rho K)}{\partial t} + \frac{\partial(\rho K U_i)}{\partial X_i} = \frac{\partial}{\partial X_j}\left[\frac{\mu_t}{\sigma_K}\frac{\partial K}{\partial X_j}\right] + 2\mu_t E_{ij}E_{ij} - \rho\epsilon \tag{10}$$

$$\frac{\partial(\rho\epsilon)}{\partial t} + \frac{\partial(\rho\epsilon U_i)}{\partial X_i} = \frac{\partial}{\partial X_j}\left[\frac{\mu_t}{\sigma_\epsilon}\frac{\partial \epsilon}{\partial X_j}\right] + C_{1\epsilon}\frac{\epsilon}{K}2\mu_t E_{ij}E_{ij} - C_{2\epsilon}\rho\frac{\epsilon^2}{K} \tag{11}$$

The Standard $K-\omega$ turbulent model was initially proposed by Wilcox [13]. This model is known as a low-Reynolds model, which means being good at predicting results in the near-wall [12]. Similar to $k-\epsilon$, This model uses twice the scalar conservation formulation but estimates $K$ and $\omega$. The turbulent kinetic energy and specific dissipation rate are solved with equation (13) and (14), respectively. The model's coefficients values are shown in table 2 while turbulent kinematic viscosity is calculated with equation (12).

$$\nu_t = \frac{K}{\epsilon} \tag{12}$$

$$\frac{\partial K}{\partial t} + U_j\frac{\partial K}{\partial X_j} = \tau_{ij}\frac{\partial U_i}{\partial X_j} - \beta^* K\omega + \frac{\partial}{\partial X_j}\left[(\nu + \sigma^*\nu_t)\frac{\partial K}{\partial X_j}\right] \tag{13}$$

$$\frac{\partial \omega}{\partial t} + U_j\frac{\partial \omega}{\partial X_j} = \alpha_\omega\frac{\omega}{K}\tau_{ij}\frac{\partial U_i}{\partial X_j} - \beta\omega^2 + \frac{\partial}{\partial X_j}\left[(\nu + \sigma\nu_t)\frac{\partial \omega}{\partial X_j}\right] \tag{14}$$

Menter proposed his Shear Stress Transport model [14], also known as $K-\omega$ SST, where it unifies the advantages of the Standard $K-\omega$ and $K-\epsilon$ models without inheriting their weaknesses [12]. Proposing a hybrid model, he reuses Reynolds stress computation and $K$-equation from Wilcox's original $K-\omega$ model and transforms the $\epsilon$-equation into a $\omega$-equation as it can be seen in equation (15). Dealing with the arising term at the most right of the equation (called *cross-diffusion term*)[10], he blended the models using equation (16) to obtain a smooth transition between them and manage the constant values of $C_1$ and $C_2$. To finally calculate the turbulent kinematic viscosity, equations (17) is used. Revised model constants are shown in table 3. The *SST* also uses the scalar conservation formulation twice, so the three previous turbulent models are classified as two-equations models.

**Table 3 Revised values for the coefficients in $K-\omega$ SST model**

| $\sigma_K$ | $\sigma_{\omega 1}$ | $\sigma_{\omega 2}$ | $\gamma_2$ | $\beta_2$ | $\beta^*$ |
|---|---|---|---|---|---|
| 1.0 | 2.0 | 1.17 | 0.44 | 0.083 | $\frac{9}{100}$ |

**Table 4 SA turbulent model constants recommended values**

| $\sigma_v$ | $\kappa$ | $C_{b1}$ | $C_{b2}$ | $C_{w1}$ |
|---|---|---|---|---|
| $\frac{2}{3}$ | 0.4187 | 0.1355 | 0.622 | $C_{b1}+\kappa^2(1+C_{b2})/\sigma_v$ |

$$\frac{\partial \rho\omega}{\partial t}+\nabla\cdot(\rho\omega U)=\nabla\cdot\left((\mu+\frac{\mu_t}{\sigma_{\omega 1}})\nabla\omega\right)+\gamma_2\left(2\rho S_{ij}-\frac{2}{3}\rho\omega\frac{\partial U_i}{\partial X_j}\delta_{ij}\right)-\beta_2\rho\omega^2+2\frac{\rho}{\sigma_{\omega 2}}\omega\frac{\partial K}{\partial X_k}\frac{\partial \omega}{\partial X_k} \tag{15}$$

$$C=F_cC_1+(1-F_c)C_2 \tag{16}$$

$$\mu_t=\frac{a_1\rho K}{\max(a_1\omega,F_2\sqrt{2S_{ij}S_{ij}})} \tag{17}$$

Very different is the SA turbulent model, proposed by Spalart and Allmaras [15] and classified as a one-equation model since it only solves for an eddy viscosity parameter $\tilde{\nu}$. The essential $\mu_t$ parameter is calculated with the equation (20), where $f_{v1}$ is a wall-dumping function that causes zero value at the wall and reaches unity at high Reynolds number cases[10]. The Reynolds stresses are calculated with the equation (19), and $\tilde{\nu}$ is computed by the scalar conservation equation (20). Where $\Omega$ is the production rate of $\tilde{\nu}$ is related to the local mean vorticity as equation (21) and (22). The Spalart-Allmaras model has earned high popularity and is often used in the aerospace and aerodynamics industry for its high reduction in computational effort. SA turbulent model constants recommended values are in table 4.

$$\mu_t=\rho\tilde{\nu}f_{v1} \tag{18}$$

$$\tau_{ij}=-\rho\overline{u_i'u_j'}=2\mu_tS_{ij}=\rho\tilde{\nu}f_{v1}\left(\frac{\partial U_i}{\partial X_j}+\frac{\partial U_j}{\partial X_i}\right) \tag{19}$$

$$\frac{\partial \rho\tilde{\nu}}{\partial t}+\nabla\cdot(\rho\tilde{\nu}U)=\frac{1}{\sigma_v}\nabla\cdot\left((\mu+\rho\tilde{\nu})\nabla\tilde{\nu}+C_{b2}\rho\frac{\partial\tilde{\nu}}{\partial X_k}\frac{\partial\tilde{\nu}}{\partial X_k}\right)+C_{b1}\rho\tilde{\nu}\tilde{\Omega}+C_{w1}\rho\left(\frac{\tilde{\nu}}{\kappa y}\right)^2f_w \tag{20}$$

$$\tilde{\Omega}=\Omega+\frac{\tilde{\nu}}{(\kappa y)^2}f_{v2} \tag{21}$$

$$\Omega=\sqrt{\frac{1}{2}\left(\frac{\partial U_i}{\partial X_j}-\frac{\partial U_j}{\partial X_i}\right)^2} \tag{22}$$

### C. Potential Flow Based Boundary Layer Detection

The terms potential flow and boundary layer rarely go together in the same sentence as by definition boundary layers are born out of viscous interactions which are not present in potential flows. A potential flow as a flow the satisfies the Laplace equation as,

$$\nabla^2\Phi=0 \tag{23}$$

where $\hat{u}=\nabla\Phi$ and $\nabla\cdot u=0$. However, in finite, floating point arithmetic the divergence of the velocity will likely be a finite value different from zero. Thus, the potential flow solver within OpenFOAM implements the solver as the Poisson equation rather than the Laplace equation as,

$$\nabla^2\Phi=\nabla\cdot\phi \tag{24}$$

where $\phi$ is the face flux of a finite volume. Given that the boundary layer can be described as the region where viscous interactions can not be neglected (a somewhat simplistic description, but it suffices for the proposed methodology) and these are not present in a potential flow, we hypothesize that the edge of the boundary layer can be detected by searching for the region where the potential flow and the real flow cross paths. In the present work, we apply the following criteria for identifying the edge of the boundary layer:

$$\frac{U_{RANS}}{U_{Potential}} \geq 1 \tag{25}$$

Figure 2 provides a pictorial representation of the intuition behind the approach employed in the present work. Note how the RANS solution tends asymptotically to the potential solution as the distance from the wall grows. Further, in the freestream, the RANS solution is consistently greater than or equal to the potential solution which leads to the criteria presented in equation 25.

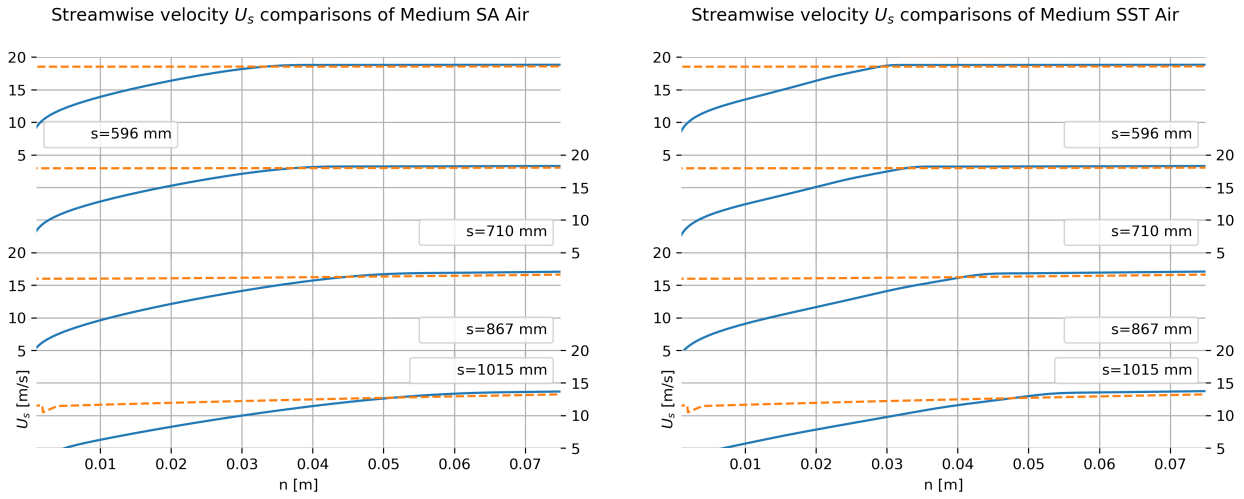


**Fig. 2 Potential Flow and RANS wall normal profiles (a) SA (b) $K-\omega$ SST. Dashed line corresponds to the potential flow solution whereas the solid line corresponds to RANS.**

### D. Numerical Details

Before beginning with the curved hill cases, a scenario of the turbulent flow over a flat plate was considered using SST and SA models. For all cases presented in this work, the classical no-slip condition was prescribed at the walls surfaces for the velocity fields; meanwhile, an isothermal condition of 293.15 K. The lateral boundary conditions were set via zero-gradient, and the only parameter with a fixed value in the outlet boundary was pressure as a zero gauge. For the SA initial conditions, the ratio $\tilde{\nu}/\nu$ was assumed to be unity since the approximation of outlet Reynolds number of $2x10^7$ while zero value at the walls. For the SST initial conditions, the turbulent intensity was presumed 1%, giving $K = 0.06$ and $\omega = 4000$ to be applied as Dirichlet conditions for the inlet and walls.

In the flat plate scenario, the domain's length was $3.85m$, although the initial $0.15m$ had slip-condition. Three meshes were designed so that for coarse, medium and fine mesh, the end-to-start cell expansion ratio were 4140, 3000 and 1900, respectively. The inlet conditions were a temperature of 323.15 K was included as a passive scalar and a horizontal velocity of $20m/s$.

In the curved hill scenario, solutions from the flat plate were injected as velocity and temperature inlet profiles to avoid the unreal freestream inlet profiles. These injecting profiles are validated, as shown further in figure [12]. The coarse mesh of the curved hill scenario had a complete vertical cells distribution of 1500 end-to-start expansion ratio. While for the medium mesh was applied 200 cells in the first 25% of vertical distance with 100 end-to-start expansion ratio

and 100 cells for the other 75% height in uniform distribution to comply with an acceptable mesh's aspect ratio. The domain was divided into five blocks; therefore, the stations' count was 250, 75, 350, 75, and 250 in streamwise order. The first and last blocks had a horizontal end-to-start expansion ratio of 0.1 and 10, respectively. The table 5 shows all meshes resolution and figures (3) and (4) examples of the computational domains. Figures (5(a)) and (5(b)) show the ZPG regions' near-wall resolution for the flat plate and curved hill, respectively.

**Table 5 Grid Nomenclature for Mesh Dimensions** (*horizontal* × *vertical*)

| Id | Flat Plate | Curved Hill |
|---|---|---|
| **Coarse** | 675 × 100 | 1000 × 200 |
| **Medium** | 900 × 134 | 1000 × 300 |
| **Fine** | 1350 × 201 | - |

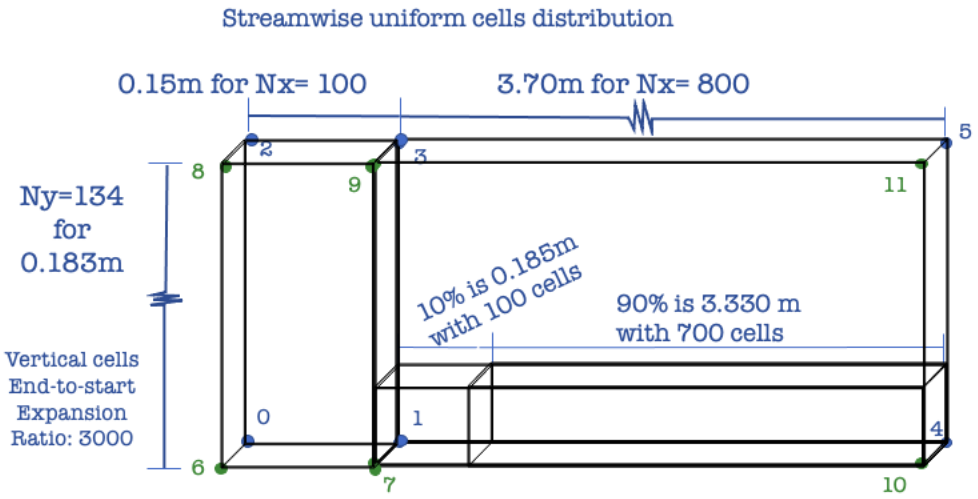


**Fig. 3 Example of dimensions and cells distribution for flat plate medium mesh.**

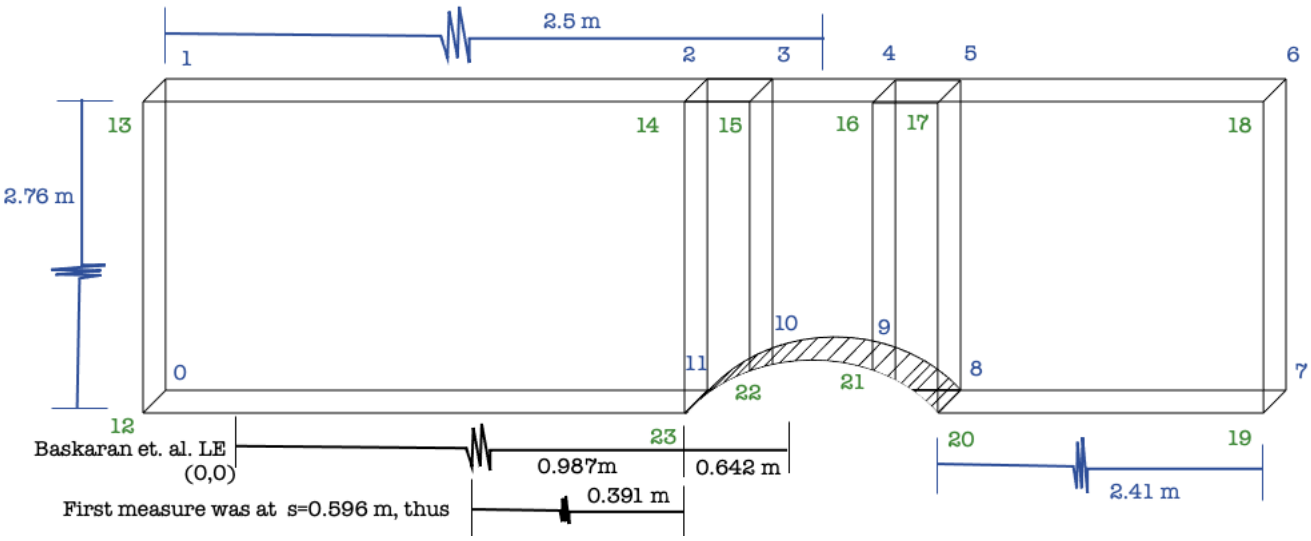


**Fig. 4 Example of dimensions of curved hill simulating [1].**

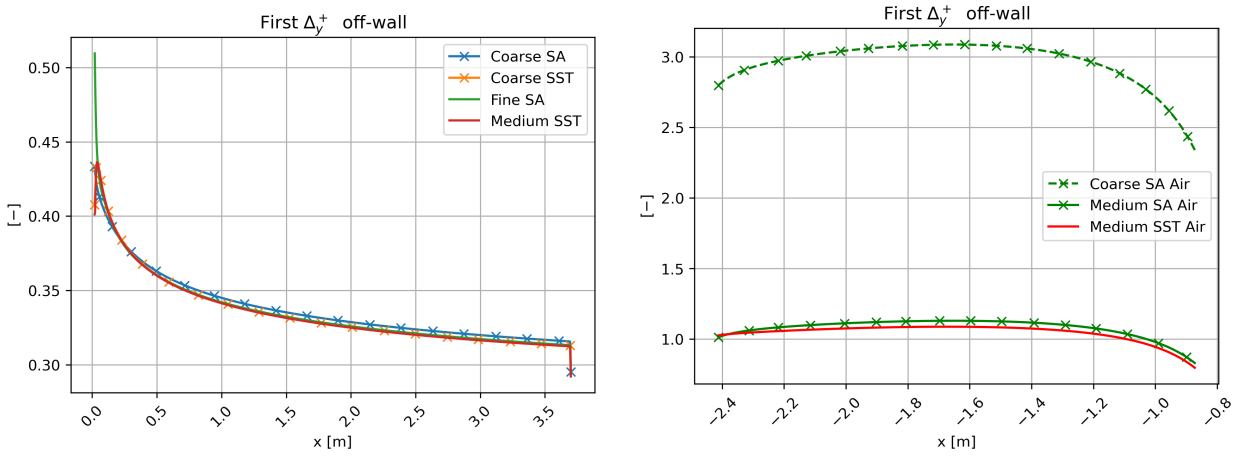


**Fig. 5 Comparison of the dimensionless near-wall mesh resolution in (a) The flat plate domain (b) The curved hill domain ZPG region.**

## IV. Preliminary Results and Discussion

The flat plate simulations have showed excellent agreement with empirical correlations. The obtained information (i.e., velocity and thermal profiles) was used to inject a more realistic boundary layer flow into the curved-hill domain inlet. Because Spalart-Allmaras cases were executed first, it was found that the results of coarse to fine mesh were sufficiently resolution-independent; therefore, SST was only performed with coarse and medium resolutions. Figure (6(a)) displays the boundary layer thickness and comparison with the One-Seventh-Power Law given in [16]. Figure (6(b)) presents the skin friction coefficient and the theoretical formulation proposed by Kays and Crawford [17]. Regarding the passive scalar solution, the temperature boundary layer thickness is shown in the figure (7(a)); as it can be seen, the results are just differentiated by the turbulent model used. Furthermore, to validate the temperature fields, the Stanton number was used in the figure (7(b)) by comparison with the theoretical formulation given by Kays and Crawford [17].

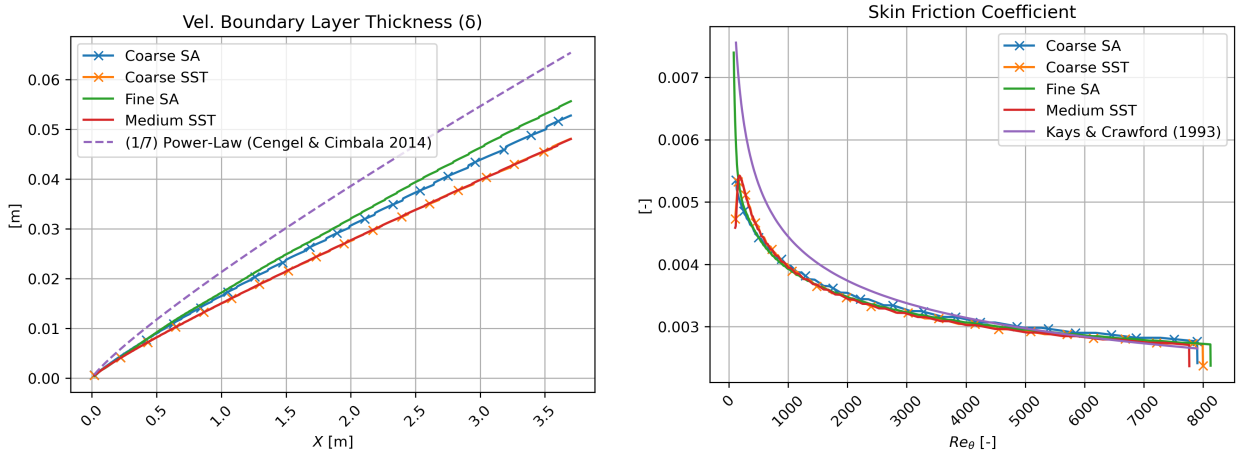


**Fig. 6 Momentum solutions for the flat plate scenario (a) Boundary Layer Thickness (b) Skin Friction Coefficient.**

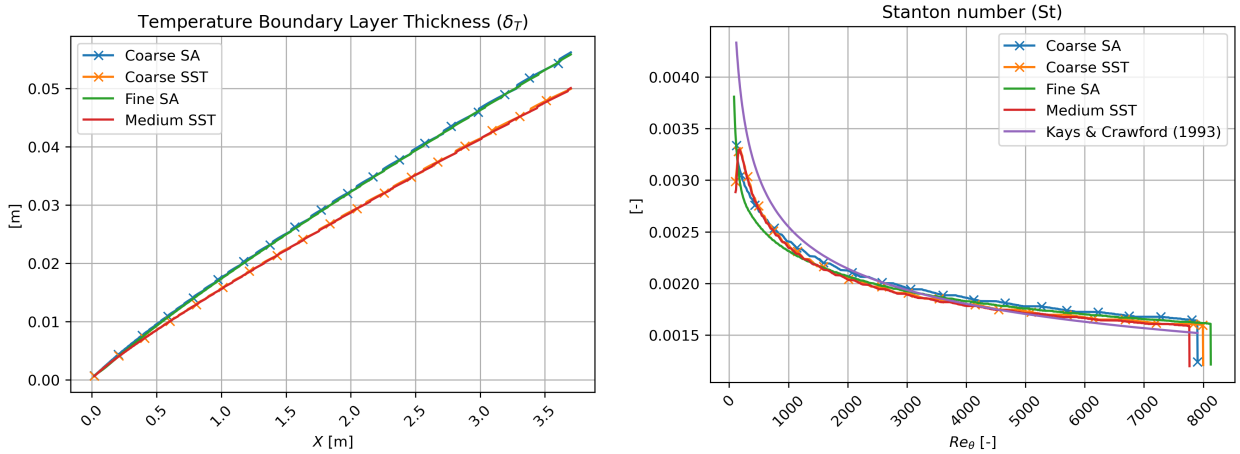


**Fig. 7 Passive scalar solution (a) Temperature boundary layer thickness (b) Stanton number.**

Entering into the curved hill scenario, let us begin by setting our bases compared with experimental data from the paper "A turbulent flow over a curved hill Part 1", [1]. In the figures 8, 9, 10 are shown the contour results of air using the SA turbulent model. It can be observed the expected behaviour of the air as turbulent flow for the kinematic pressure gauge, streamwise velocity and temperature parameters, respectively. Very important to note that in this work the surface streamline distance ($s$) was matched to the presented in [1], also the wall-normal distance is represented with $n$. In the path of the near-wall region, the following aspects can be mentioned. As the flow approaches the hill or obstacle, the pressure increases and the pressure gradient becomes strongly adverse. The fluid velocity in the viscous and buffer layer decelerates, inducing a decrease of the skin friction coefficient, as will be shown later in the manuscript. However, not strong backflow or reverse flow is seen due to the moderate APG infringed. Whereas, the temperature generally shows a small gradient with just a small temperature drop in a very limited location at the peak of this pressure strong adverse gradient. In the geometry change from concave to convex, the pressure gradient switches to favorable (FPG), this is translated to streamwise velocity acceleration. This flow acceleration or FPG continue until the flow reach the top's hill. Clearly, the flow decelerates downhill, with a significant recovery of the pressure coefficient (as seen in fig. 11 (left)). The presence of this strong APG (the pressure increase equals the dynamic pressure, since the change in $C_p \approx$ -1) ends it up in flow separation, with a posterior flow reattachment due to the presence of zero pressure gradient (ZPG)

again. Temperature shows no change during this section with the exception in the very near wall where is a very small temperature drop. Here, the pressure gradient is still favorable but with lower magnitude similarly the velocity continues its direction but with almost half magnitude. At the start of this separation zone, temperature begins to drop. At the end of the hill, the separation “bubble” is noticeable due to the presence of an iso-thermal zone. The high level of mixing inside the separation bubble balances the static temperature. This is consistent observations in the thermal boundary layer downstream of crossflow jet problems via DNS [18].

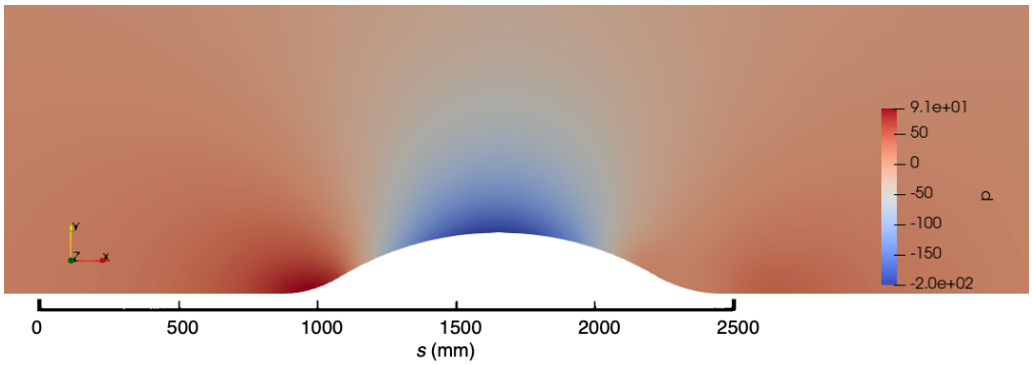


**Fig. 8 Kinematic pressure gauge field contour of air with SA model; the contour has been "zoomed in" to highlight the curved hill and immediate surroundings.**

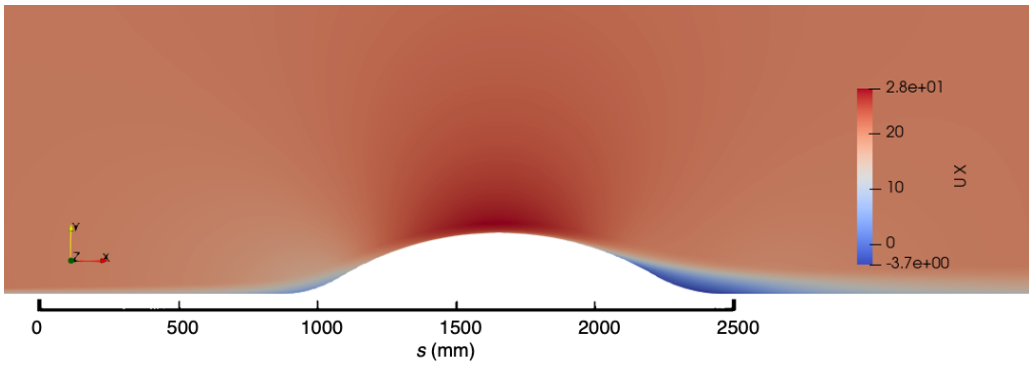


**Fig. 9 Streamwise velocity field contour of air with SA model; the contour has been "zoomed in" to highlight the curved hill and immediate surroundings.**

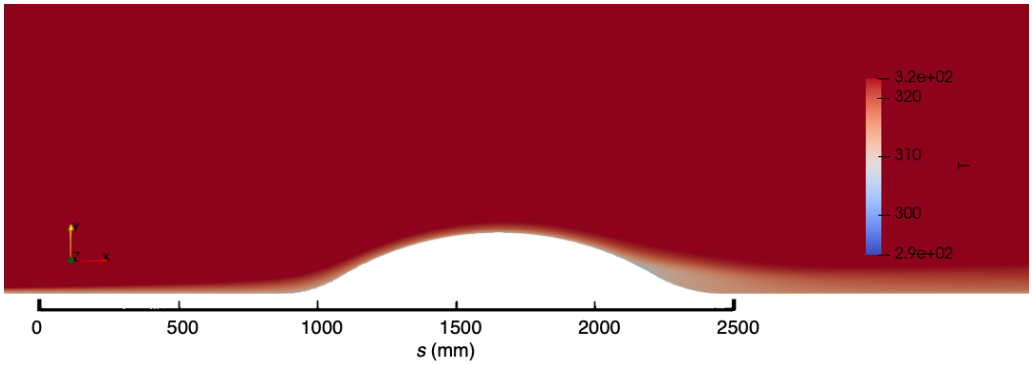


**Fig. 10 Temperature field contour of air with SA model; the contour has been "zoomed in" to highlight the curved hill and immediate surroundings.**

Figure 11 (left) depicts the pressure coefficient along the computational domain. The pressure coefficient is defined as $C_p = (P_w - P_\infty)/q_\infty$. Here, $P_w$ is the wall static pressure, $P_\infty$ is the fresstream static pressure and $q_\infty$ is the freestream dynamic pressure. In general, a fair agreement is observed with experimental data by [1]. Most of the discrepancies occurs at the top of the curved hill. Future assessment will involve local mesh refinement and the evaluation of the SA turbulence model. Furthermore, it can be noted that regarding the pressure coefficient in Figure 11 (left) the peak occurs at what is called the feet of the hill. In Figure 11(right), the skin friction coefficient, $C_f$, is depicted. The skin friction coefficient is defined as follows, $C_f = \tau_w/q_\infty$, where $\tau_w$ is the wall shear stress. One can observe an opposite trend of $C_f$ as compared with the pressure coefficient $C_p$. As the flow decelerates due to the presence of moderate APG upstream the curved hill, it is seen a decreasing behavior of $C_f$. However, it never reaches negative values, indicating that the mean flow does not separate. At roughly one quarter of the curved hill (where surface change geometry from concave to convex) a meaningful increase of the wall shear stress and $C_f$ is observed, approximately a 70% increase with respect to incoming flow conditions. Downstream, the pressure coefficient recovery induces a reduction in $C_f$, to finally reaches slightly negative values in the separation bubble.

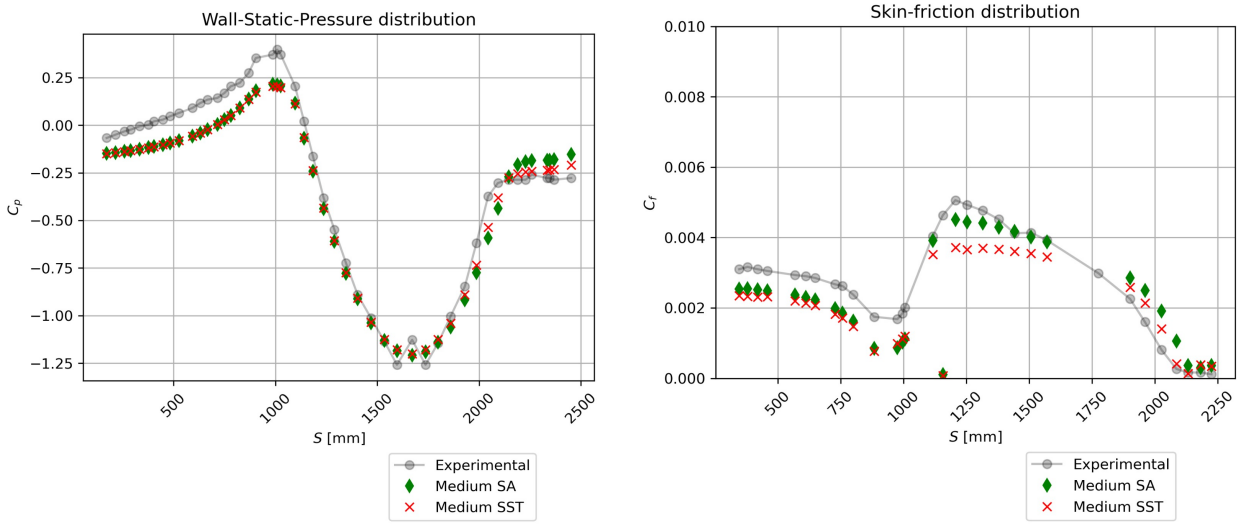


**Fig. 11 (Left) Pressure coefficient at wall surface compared to experimental data from [1]; (Right) Skin friction coefficient at wall surface compared to experimental data from [1]; both employ the SA model.**

To assess the distortion of the boundary layer (both momentum and thermal) due to the hill, we present wall normal, inner scaled profiles and compare our results against two DNS baselines by Schlatter & Orlu ($Re_\theta = 4061$) [8] and

Lagares & Araya ($Re_\theta = 2305$) [7] in figure 12. The inner scaled velocity profiles of both closure models considered collapse near perfectly with a very slight variation observed in the log region where the $K-\omega$ SST variant predicts a slightly higher velocity. The boundary layer suffers a significant distortion midway through the first concave portion of the hill where a plateau can be observed between $y^+ = 30$ and 100. Furthermore, the acceleration induced by the FPG produces a velocity profile resembling that of a laminar boundary layer suggesting the acceleration is strong enough to produce a laminarescent state; however, further investigation is required to prove the validity, or lack thereof, of this hypothesis. In spite of this, we reinforce the hypothesis of a laminarescent state near the top of the hill by visualizing the Reynolds shear stresses. We apply the Boussinesq hypothesis to estimate these from the RANS output as per equation 26. The turbulence models tend to capture the inner portion of the boundary layer with very good agreement to the DNS validation data. The comparison breaks down in the log region where both models predict a sharp drop. There is an appreciable attenuation in the Reynolds shear stresses near the top of the hill that suggests the flow is quasi-laminarized or at the verge of relaminarization given the stresses in the incoming flow are 1.62 times larger based on the SST prediction (1.51 times for the SA model) than those at the top of the hill [19]. Finally, the sudden deceleration of the boundary layer produces a recirculation bubble above the wall, i.e. between 2 to 800 wall units, as can be seen in fig. 12. The SA model predicts a stronger reversal whereas the SST model predicts a larger (in terms of wall normal distance) bubble. The separation point as predicted by the $K-\omega$ SST can be found at $s = 2136$mm (roughly 1.95% error as compared to the experimental data by Baskaran *et al.* [1]). The SA model predicts a slightly delayed reversal at $s = 2169$mm (approximately 3.5% error against the same experimental baseline). The thermal boundary layer presented in fig. 12(b) follows a similar tendencies to those presented for the momentum boundary layer. This is expected since temperature is modelled as a passive scalar. Once again, thermal boundary layer resembles a laminarescent state in the center portion of the hill. Although the separation bubble affects the thermal boundary layer, the effects are less "violent" than those seen in the momentum boundary layer. The separation bubble seems to elongate the thermal plateau and the predictions of both turbulence models seem to disagree more than on any other section. Further studies are required (at the LES and/or DNS level) to better understand the detached flow region. The published data by Baskaran *et al.* does not contain much information beyond the early portions of the separation bubble [1].

$$(u'v')^+ \approx -\left(\frac{\nu_T}{u_\tau^2}\right)\left(\frac{\partial U_s}{\partial n} + \frac{\partial U_n}{\partial s}\right) \tag{26}$$

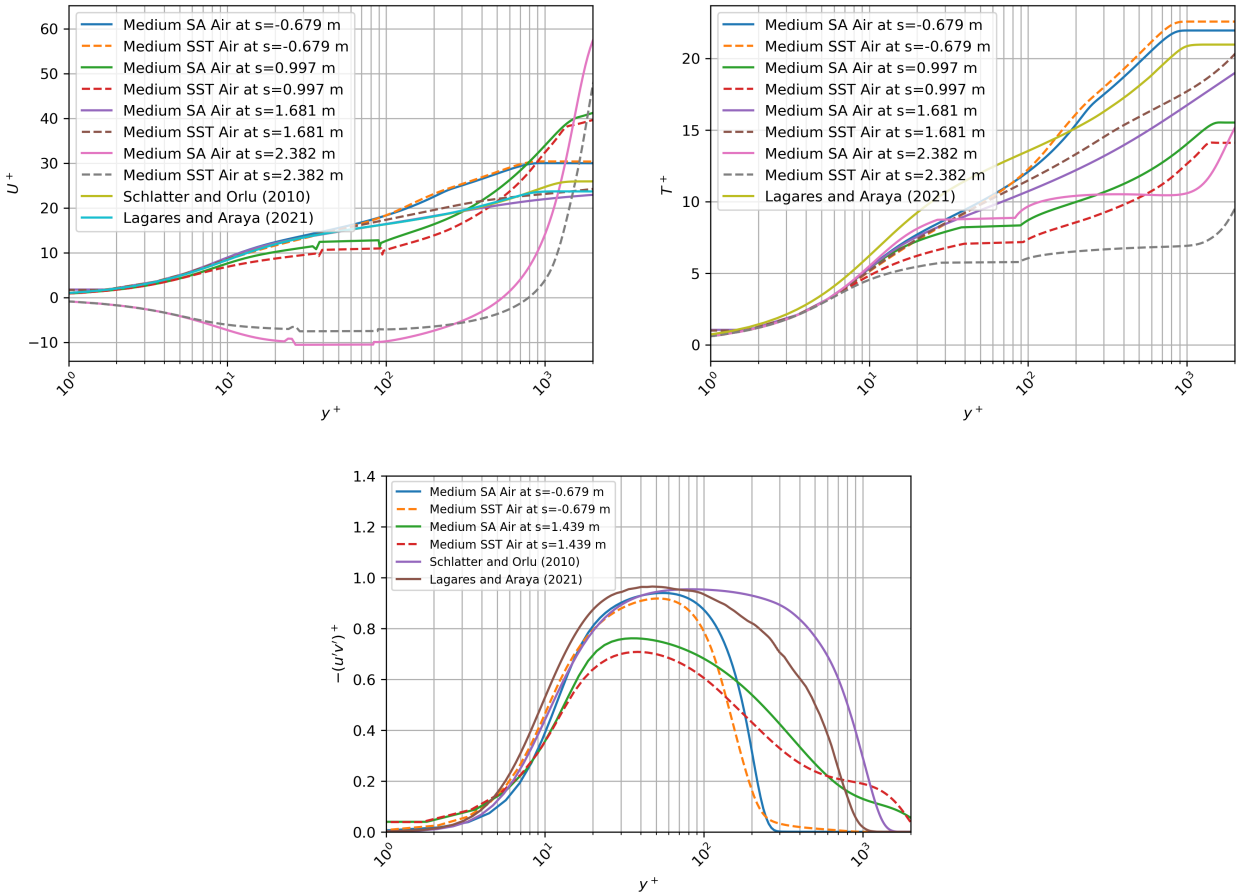


**Fig. 12 Momentum and thermal boundary layers (a) Inner-scaled velocity (b) Inner-scaled temperature (c) Inner-scaled Reynolds shear stresses**

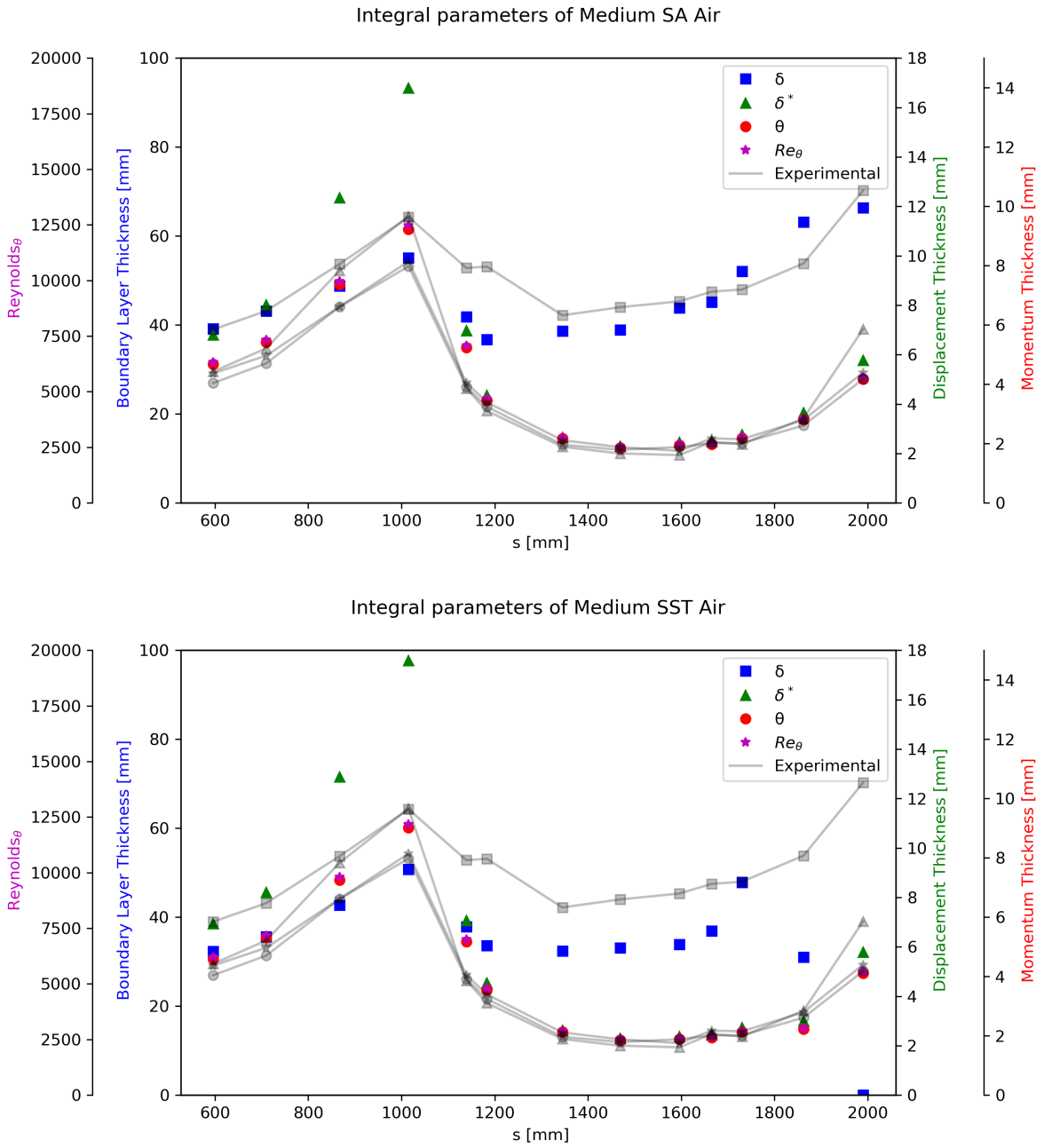


**Fig. 13 Integral parameters, Momentum Thickness Reynolds Number and Boundary Layer Thickness compared to experimental data from [1]; (top) Spalart-Allmaras model; (bottom) $K-\omega$ SST model.**

The boundary layer thickness (naturally) and the integral parameters went through a dramatic benefit from changing from the traditional boundary layer edge detection based on $99\%U_\infty$ to our potential flow-based scheme. This made the overall calculation of the parameters shown in figure 13(top) robust in the presence of strong pressure gradients and strong boundary layer distortion. The boundary layer thickness is slightly underestimated in the transition from the first concave portion to the convex section where a slight over estimation is then seen. Baskaran *et al.* has limited data in the separation bubble, and we focus on the sections highlighted by them [1]. The overestimated displacement thickness is likely due to an overestimation in the boundary layer's edge velocity incurred when comparing the potential and RANS flow fields. Nonetheless, the comparisons along the hill are extremely favorable to our approach as compared to the

experimental baseline. Overall, the SA model has a superior performance when compared to the $K-\omega$ SST [14]. This is particularly noticeable in the closer agreement in the convex portion seen in the boundary layer thickness prediction. The over estimation of the integral parameters is also less drastic at the feet of the hill.

## V. Future Work and Next Steps

Additional sources of validation will be included to better characterize the performance of the considered model in strong pressure gradients. Further, we will be extending this study to a 3D geometry and conduct a large eddy simulations to better understand the unsteadiness of the detached boundary layer and the laminarescent state that we have hypothesized. Also, we will further investigate the proposed approach for boundary layer detection and its resiliency in more complex geometries and stronger pressure gradients. One important variable not considered in this study in its current form is the effect of the curvature driven pressure gradients on the thermal boundary layer as a function of $Pr$.

## VI. Conclusions

We have presented a numerical study of a turbulent boundary layer subject to a curved hill. The study was limited to a Reynolds Averaged Navier Stokes simulation, and the domain was reproduced following work by Baskaran *et al.* [1]. The inlet velocity profile was recycled from a precursor ZPG simulation to avoid a longer transient in the presented RANS cases. We showed very good agreement with experimental data by Baskaran *et al.* [1] by leveraging a boundary layer identification scheme based on a potential flow field. This approach led to better agreement with the experimental data points in the integral parameters and boundary layer thickness and was resilient in the presence of strong pressure gradients and significant boundary layer distortion. The SA model had a better agreement with the experimental data, although we highlight a slight superiority of the SST model in the transition to the APG region and its prediction of the separation point. The SA model had a better performance in the presence of strong favorable pressure gradients that we hypothesized could have induced a laminarescent state along the FPG. We also highlighted the more notable effect of the detachment on the velocity profile than the thermal profile but did note the notable differences in predictions between the considered models. However, more data is needed to objectively judge their overall accuracy in the separation bubble.

## Acknowledgments

This material is based upon work supported by the National Science Foundation under Grant No. HRD-1906130 and Grant No. 1847241.

## References

[1] Baskaran, V., Smits, A., and Joubert, P., "A turbulent flow over a curved hill Part 1. Growth of an internal boundary layer," *Journal of Fluid Mechanics*, Vol. 182, 1987, pp. 47–83.

[2] Menter, F. R., "Two-equation eddy-viscosity turbulence models for engineering applications," *AIAA Journal*, Vol. 32, No. 8, 1994, pp. 1598–1605. https://doi.org/10.2514/3.12149.

[3] Spalart, P., and Allmaras, S., "A one-equation turbulence model for aerodynamic flows," *30th Aerospace Science Meeting and Exhibit, Reno, NV, USA*, Vol. AIAA Paper 92-0439, 1992.

[4] Li, Q., Schlatter, P., Brandt, L., and Henningson, D. S., "DNS of a spatially developing turbulent boundary layer with passive scalar transport," *International Journal of Heat and Fluid Flow*, Vol. 30, No. 5, 2009, pp. 916–929.

[5] Moukalled, F., Mangani, L., Darwish, M., et al., *The finite volume method in computational fluid dynamics*, Vol. 113, Springer, 2016.

[6] Lagares, C. J., Rivera, W., and Araya, G., "Aquila: A Distributed and Portable Post-Processing Library for Large-Scale Computational Fluid Dynamics," *AIAA SciTech*, 2021.

[7] Lagares, C. J., and Araya, G., *Compressibility Effects on High-Reynolds Coherent Structures via Two-Point Correlations*, 2021. https://doi.org/10.2514/6.2021-2869, URL https://arc.aiaa.org/doi/abs/10.2514/6.2021-2869.

[8] P. Schlatter and R. Orlu, "Assessment of direct numerical simulation data of turbulent boundary layers," *Journal of Fluid Mechanics*, Vol. 659, 2010, pp. 116–126.

[9] Mollicone, J.-P., Battista, F., Gualtieri, P., and Casciola, C. M., "Effect of geometry and Reynolds number on the turbulent separated flow behind a bulge in a channel," *Journal of Fluid Mechanics*, Vol. 823, 2017, pp. 100–133.

[10] Versteeg, H. K., and Malalasekera, W., *An introduction to computational fluid dynamics: the finite volume method*, Pearson education, 2007.

[11] Launder, B. E., and Spalding, D. B., "The numerical computation of turbulent flows," *Numerical prediction of flow, heat transfer, turbulence and combustion*, Elsevier, 1983, pp. 96–116.

[12] Lee, C.-H., "Rough boundary treatment method for the shear-stress transport k-$\omega$ model," *Engineering Applications of Computational Fluid Mechanics*, Vol. 12, No. 1, 2018, pp. 261–269.

[13] Wilcox, D. C., "Reassessment of the scale-determining equation for advanced turbulence models," *AIAA journal*, Vol. 26, No. 11, 1988, pp. 1299–1310.

[14] Menter, F. R., "Two-equation eddy-viscosity turbulence models for engineering applications," *AIAA journal*, Vol. 32, No. 8, 1994, pp. 1598–1605.

[15] Spalart, P., and Allmaras, S., "A one-equation turbulence model for aerodynamic flows," *30th aerospace sciences meeting and exhibit*, 1992, p. 439.

[16] Cengel, Y. A., and Cimbala, J. M., *Fluid Mechanics: Fundamentals and Applications*, McGraw-Hill Education, 2014.

[17] Kays, W. M., and Crawford, M. E., *Convective Heat and Mass Transfer*, Vol. 3rd ed., McGraw-Hill, New York., 1993.

[18] Quinones, C., "Transport Phenomena in Crossflow Jets Subject to Very Strong Favorable Pressure Gradient," *MSc thesis, University of Puerto Rico-Mayaguez*, 2020.

[19] Narasimha, K., R. & Sreenivasan, "Relaminarization of fluid flows," *Advances in Applied Mechanics*, Vol. 19, 1979, pp. 221–309. https://doi.org/10.1016/S0065-2156(08)70311-9.